Insights into the Structure and the Electrochemical Reactivity of Cobalt-Manganese Layered Double Hydroxides: Application to H2O2 Sensing

Hani Farhat, Christine Taviot-Gueho, Guillaume Monier, Valérie Briois, Claude Forano, Christine Mousty

Insights into the Structure and the Electrochemical Reactivity of Cobalt-Manganese Layered Double Hydroxides: Application to H_2O_2 Sensing

Hani Farhat[a], Christine Taviot-Gueho[a], Guillaume Monier[b], Valérie Briois[c], Claude Forano*[,a] and Christine Mousty*[,a]

[a] Université Clermont Auvergne, CNRS, SIGMA Clermont, Institut de Chimie de Clermont-Ferrand, F-63000 Clermont–Ferrand, France.

[b] Université Clermont Auvergne, CNRS, SIGMA Clermont, Institut Pascal, F-63000 Clermont–Ferrand, France.

[c] Synchrotron SOLEIL, CNRS-UR1, BP 48, L'orme des Merisiers, 91192 Gif-sur-Yvette, France.

CoRMn LDH_J Phys Chem C_SI.pdf

ABSTRACT: A series of Co_RMn-LDH (R = 1, 2, 3, 4, 5) was synthesized by the coprecipitation method. The formation of layered double hydroxides (LDH) phases is confirmed by powder X-ray diffraction (XRD) and infrared spectroscopy (FTIR). The energy dispersive X-ray analysis (EDX) shows the total coprecipitation of Co and Mn. The X-ray photoelectron spectroscopy (XPS) gives evidence of the joint presence of Co(II), Co(III) and Mn(III) in the LDH structures in proportion depending on the initial R value. The Rietveld refinement of the structure using the XRD data reveals that the sample with a CoMn ratio 3:1 displays a pure LDH phase containing mainly Co(II) and Mn(III) with a M(II)/M(III) of nearly 2.1, in agreement with the X-ray absorption spectroscopy (XAS) results at the Co and Mn K-edges, strong hydrogen bonding network involving CO_3^{2-}/OH^- charge compensating anions in the interlayers. When compared with the other Co_RMn-LDH, the Co_3Mn-LDH displays the best redox properties in an alkaline medium (0.1 M NaOH) and in a neutral pH (Tris buffer). An in-depth study of the Co_3Mn-LDH obtained after electrochemical oxidation was also performed. The evolution of Co and Mn oxidation state under electrochemical oxidation were evidenced by XPS. Finally, the performance of the Co_3Mn-LDH modified electrode was determined for the electrocatalytic detection of hydrogen peroxide.

INTRODUCTION

Among the nanomaterials reported in the literature for various electrochemical applications[1-3], layered double hydroxides (LDH) are mentioned as emerging materials. LDH are two-dimensional (2D) materials made by the stacking of positively charged brucite-like layers separated by intercalated charge-compensating anions and water molecules. They are represented by the general formula $[M^{2+}_{1-x}\ M^{3+}_x(OH)_2][X^{m-}_{x/m}, nH_2O]$ with M^{2+} and M^{3+} being divalent and trivalent metal cations, respectively and X^{m-} the anionic species. Owing to their adjustable chemical composition, concerning both the metal cations (M^{2+}, M^{3+}, M^{2+}/M^{3+}) in the hydroxide layers and the intercalated anions (X^{m-}), LDH display modulating electrochemical properties. Moreover, thanks to the recent progress in synthesis and particle structuration, LDH materials can be processed in different ways, such as well-defined nanoparticles, exfoliated nanosheets, nano- or hollow spheres, thin films coated onto planar substrates or various 3D macroporous scaffolders leading to anisotropic materials with high surface area and enhanced diffusional properties.

LDH containing transition metals (TMs) (Ti, V, Mn, Fe, Co, Ni, Cu) are, since very recently, under great investigation for energy conversion and storage[4-6], such as pseudo-capacitors[7-8], $Li-O_2$ batteries[9] or electrocatalysts for water splitting[10-14], as well for electroanalytical applications.[15] Indeed, the LDH structure is a unique

structure that can combine mixed-valent TM cations (NiFe, NiCo, CoMnTi, CoNiFe, etc.) in its framework. In many cases, the combination of two to three different TM cations promotes a synergistic effect that improves the electroactivity of the multicomponent LDH compared to the LDH based on a single TM[13, 16]. While this synergistic effect has been reported in many studies[7], a clear understanding of the fundamental phenomena involved (change in the electronic structure, band gap, electron hopping pathway, etc.) is still missing.[13, 16]

In the other hand, hybrid and biohybrid materials or nanocomposites based on LDH, with unique electrocatalytic properties, have been used as electrode modifiers in electrochemical sensing applications for the determination of environmental pollutants or small biomarkers, such as glucose or hydrogen peroxide[1-3, 17-21]. Hydrogen peroxide (H_2O_2) is a small molecule which has key implications in various industrial or biomedical processes.[22] It is a product generated from biochemical reactions catalyzed by oxidoreductase enzymes, such as glucose oxidase (GOx). Besides its toxicity for living cells, hydrogen peroxide has been considered as a probe molecule for recognition of oxidative stress. Moreover, *in vitro* determination of H_2O_2 is of great importance as H_2O_2 is a biomarker for the diagnosis of cancer. Therefore, H_2O_2 detection is crucially important for both academic and industrial purposes.[23] This molecule can be either oxidized or reduced by electrochemistry, but for analytical purposes, modified electrodes are generally used to decrease the overpotential and to increase the electron transfer kinetics. As recently reported in the literature[2-3, 24-25], both enzymatic and non-enzymatic LDH modified electrodes have been applied for sensing H_2O_2. Indeed, hemoprotein@LDH biohybrids, peroxidase-like LDH hybrids and LDH nanocomposites based on metal oxide nanoparticles (NPs), silver NPs or nanodentrites (NDs) are reported to be good electrocatalysts for H_2O_2 reduction in neutral pH. However, considering the negative potentials required for a sensitive detection of H_2O_2, most of these sensors must be used under a N_2 saturated atmosphere to avoid interference with oxygen reduction. This can be a limitation for the development of an enzymatic biosensor based on an oxidoreductase using O_2 as a cofactor, such as GOx. Recently, it was reported in the literature, that TMs (Ni or Co) based LDH exhibit good electrocatalytic properties for H_2O_2 oxidation in basic medium[26-27]. Redox molecules, i.e. iron porphyrin[28], naphthol green B[29], or carbon nanotubes (MWCNts)[30] can be added into CoAl multilayer structures to serve as an electron relay and then improve the electrocatalytic process.

Due to the combination of mixed valence states of cobalt and manganese, CoMn-LDH have demonstrated interesting electrochemical properties as oxygen evolution catalysts[14, 31-33] and pseudo-supercapacitors[34-36]. However, so far, only Xu et al.[37] mention the use of CoMn-LDH combined with gold nanoparticles (AuNPs) for H_2O_2 electrodetection. They have reported that CoMn-LDH is a good support for the electrodeposition of AuNPs. The resulting AuNPs/CoMn-LDH nanocomposite was successfully applied to H_2O_2 detection in neutral pH. Moreover, metal oxides, such as manganese oxide or cobalt oxide, are also reported as promising candidates for H_2O_2 sensing, in replacement of expensive noble metals.[23]

Inspired by these considerations, we have prepared a series of Co_RMn-LDH with different Co/Mn ratios (R = 1, 2, 3, 4, 5). The synergistic effect of such metal combinations on the structural characteristics of the LDH materials and their electrochemical properties in an alkaline electrolyte (0.1 M NaOH) were investigated. The electrocatalytic properties of Co_RMn-LDH modified electrodes concerning H_2O_2 detection was then studied in Tris buffer solution pH 7.

EXPERIMENTAL SECTION

Chemicals. The reagents used for the preparation of the LDH phases, cobalt nitrate hexahydrate ($Co(NO_3)_2 \cdot 6H_2O$, 98%), manganese nitrate tetrahydrate ($Mn(NO_3)_2 \cdot 4H_2O$, 97%) and sodium carbonate (Na_2CO_3) were purchased from Honeywell and sodium hydroxide (NaOH, 98%) from Acros. The electrolyte solutions were prepared with hydrochloric acid (HCl 37%) from Acros

and Trizma base (Tris(hydroxymethyl) aminomethane, 99.9%) from Sigma-Aldrich. Hydrogen peroxide (H_2O_2, 35 wt,% solution in water) was purchased from Acros. The interfering molecules used in the electrochemical study were α-D(+)-Glucose ($C_6H_{12}O_6$, 99% anhydrous, Acros), sodium phosphate tribasic dodecahydrate ($Na_3PO_4.12H_2O$, ≥98%), (+)-sodium L-ascorbate ($NaC_6H_7O_6$ crystalline, ≥98%), sodium acetate (CH_3COONa, ≥99%) from Sigma-Aldrich. All these chemicals were used as received without further purification. Deionized water was employed for all experiments.

Synthesis. The Co_RMn-CO_3 LDHs were synthesized using the co-precipitation method. Typically, 100 mL of a mixed $Co(NO_3)_2.6H_2O$ and $Mn(NO_3)_2.4H_2O$ solution, with a total metal concentration equal to 0.16 M and R = Co(II)/Mn(II) molar ratio equal to 1, 2, 3, 4 and 5, was added to 100 mL of a basic 0.2 M NaOH/0.1 M $NaCO_3$ solution, previously purged for 1 h with N_2. Addition was conducted over a period of 20 min in an N_2 atmosphere and under a vigorous stirring. Volumes and concentrations were previously adjusted in order to reach a final pH of 10.0. Crystallization was favored thanks to the use of a reflux at 50 °C. The resulting precipitates were washed with deionized water and centrifuged three times, and finally dried at room temperature in the dark for 12 h. The as-obtained products were labelled Co_RMn-CO_3 with R = 1, 2, 3, 4, 5 (also abbreviated as $1 \leq R \leq 5$).

Characterizations. X-ray diffraction analyses were performed using theta-theta PANalytical X'Pert Pro diffractometer equipped with a Cu anticathode ($\lambda K\alpha_1$ = 1.540598 Å, $\lambda K\alpha_2$ = 1.544426 Å) and an X'Celeretor detector. For the phase identification and refinement of the unit cell parameters of the series of Co_RMn-CO_3 samples, patterns were recorded in the range 3 - 90°/2θ with a step size of 0.033422°. For the structural and microstructural investigation of Co_3Mn-CO_3, data were recorded up to 120°/2θ with a step size of 0.008355°. The instrumental resolution function of the diffractometer was determined with an Y_2O_3 standard (U =0.027834 deg^2, V =−0.072321 deg^2, W = 0.046085 deg^2, X = 0.103318 deg^2, Y = 0.032418 deg^2). Whole powder pattern fitting was performed using the software package FullProf[38] and the pseudo-Voigt function modified by Thompson-Cox-Hastings was used as the peak profile function.[39] The background was refined by adjusting the height of pre-selected points for linear interpolation. Anisotropic size broadening was modelled in terms of spherical harmonics[40], and the average apparent crystallite size was calculated along [00l] and [110] directions assimilated respectively to the thickness L_{00l} and the in-plane L_{110} dimensions of the LDH hexagonal platelets. The structural refinement was carried out taking as initial parameters those reported recently by Zhitova et al. for the single crystal structure of $Mg_6Al_2(OH)_{16}(CO_3)(H_2O)_4$.[41] Fourier transform infrared (FTIR) spectra were recorded in transmission mode using the KBr pellet technique (2 % weight) with a Nicolet 5700 spectrometer from Thermo Scientific over the wavenumber domain from 400 to 4 000 cm^{-1} with a scan number of 128 at a resolution of 4 cm^{-1}. Scanning electron microscopy (SEM) images were recorded using a JSM-7500F Field Emission Scanning Electron Microscope operating at an acceleration voltage of 3 KV and magnifications of x500, x5,000, x50,000. Samples to be imaged were mounted on conductive carbon adhesive tabs and coated with a gold thin layer. The SEM images of the Co_3Mn-LDH films were recorded directly on a carbon electrode. Energy-dispersive X-ray spectroscopy (EDX) was performed using the same apparatus with an acceleration voltage of 20 kV and Cu as a calibration standard. Transmission electron microscopy (TEM) images were taken using a Hitachi 7650 microscope at an acceleration voltage of 80 kV. One droplet of the aqueous colloidal suspension of Co_3Mn-LDH was deposited on a 400 mesh holey carbon-coated copper grid and dried at room temperature. Thermogravimetric analyses (TGA) were made using a Setaram 92-16.16 under air flow (20 mL.min^{-1}) in the temperature range of 25-1500°C with a linear temperature ramp of 5 °C per min. X-ray photoelectron spectroscopy (XPS) measurements were performed in an ultrahigh

vacuum photoelectron spectrometer equipped with an Omicron DAR 400 X-ray source and an Omicron EA 125 hemispherical analyzer. The Mg Kα source (1253.6 eV) running at 300 W is separated from the analyzer by an angle of 55°. A medium magnification mode and constant pass energy of the analyzer equal to 20 eV were used for analysis. Photoelectron data were recorded at a take-off angle of 90° (normal detection). The survey spectrum and the high-resolution spectra were recorded with an energy step of 0.5 eV over 1200 eV and 0.1 eV, respectively. The electron binding energies (E_b) of the Co2p, Mn2p, and O1s core levels were corrected according to the electrostatic charges which was assumed to be equal to the difference between the measured binding energy of the M-OH species in the O1s and the reference value of 531.2 eV[42-43]. The presence of overlapping contributions of carbonate of Co and Mn in the C1s peak complicates the usual energy referencing to the C-C and C-H bonds of adventitious carbon, which seem to have a different charge level depending on the composition of Co_RMn-LDH. Binding energies, line widths and areas of the different XPS peaks were obtained by a weighted least squares fitting of a Lorentzian-Gaussian model curve to the experimental data using the program XPSPEAK41. The atomic percentages were obtained using the empirical formula of XPS signal intensity[44] considering a homogeneous atomic concentration and the accurate spectrometer calibration described in reference[45]. XANES and EXAFS measurements at the Co (7709 eV) and Mn (6539 eV) K-edges were performed at the ROCK beamline (SOLEIL synchrotron)[46], using the Si(111) Quick-EXAFS monochromator with the main goniometer aligned at 14.50 ° and 16.45° for an oscillation amplitude of 2.0° and 3.1°, respectively. Mirrors with a B_4C coating and a grazing incidence of 2.8 mrad with respect to the pink and monochromatic beams were used for harmonic rejection. For the pristine LDH prepared as pellets diluted in boron nitride, data were collected at both edges in transmission mode using 3 ionization chambers filled with nitrogen, the two first ionization chambers are used for measuring the sample transmission whereas the second and third ones are used for collecting the signal of manganese and cobalt reference foils. The LDH thin film electrodes prepared for cyclic voltammetry (CV) were characterized at both edges after CV using a home-made electrochemical cell available at the beamline[47]. In that case, measurements were carried out in fluorescence mode using a solid-state Passivated Implanted Planar Silicon (PIPS) detector from Canberra, Inc. located at a right angle with respect to the incident X-ray beam. The electrochemical cell with the working electrode was tilted to 45° compared to the incident X-ray beam towards the PIPS in order to allow fluorescence collection. Oscillation frequency of the crystal was chosen at 2Hz giving rise per second of 2 spectra collected with ascending Bragg angles and 2 spectra collected with descending Bragg angle. In order to improve the Signal to Noise ratio, 3000 to 3600 spectra recorded successively were merged for the pellets and 1100 spectra for the thin film electrodes. Normalization of the XAS spectra was performed using the Python normal_gui graphical interface developed at the beamline for the fast handling of the Quick-XAS data[48]. EXAFS least square fitting was performed using IFEFFIT[49] available with Horae package[50]. The amplitude reduction factor, S_0^2, and energy parameter, were derived using EXAFS analysis and fitting of Co_3O_4 and Mn_2O_3 for which crystallographic structures are known.

Electrochemical measurements. All cyclic voltammograms (CVs) were carried out with a potentiostat Autolab PGSTAT204 controlled by the NOVA software (Metrohm). The experiments were made in 0.1 M NaOH and 0.1 M Tris buffer solution (pH 7) solutions using a three electrode cell, including a Ag-AgCl electrode as the reference electrode, a platinum auxiliary electrode and a pyrolytic graphite electrode (0.07 cm^2 PGE) coated with LDH thin films as the working electrode. Before deposition, the electrode surface was polished with 1 µm diamond paste and washed with acetone and then polished again with 0.04 µm alumina slurry to be finally rinsed with ethanol and water. A drop (10 µL) of a 2 mg/mL LDH suspension (20 µg) stirred over-

night was deposited on the electrode surface and dried in a desiccator for 3 h. GCE and carbon paper electrodes with 1 cm^2 area were used to prepare the oxidized Co_3Mn-LDH for XPS and XAS characterization, respectively, the same LDH surface density (≈ 300 μg cm^{-2}) was deposited on these electrodes. Electrochemical Impedance Spectroscopy (EIS) measurements were recorded with the pristine and the oxidized LDH coatings using a BioLogic Science Instruments SP-150 with a potential modulation of 10 mV (peak to peak) in a frequency range between 25 mHz to 100 KHz. The data were recorded at the initial open circuit potential (OCP_i) and at 0.3 V/Ag-AgCl after CV 5 cycles in 0.1 M NaOH. The Nyquist plots were fitted with EC-Lab software using the equivalent circuit model previously proposed for CoAl-NO_3 and NiAl-NO_3 LDH samples.[51] Chronoamperometry experiments were recorded with a potentiostat EA161 (EDAQ), under stirring conditions at an applied potential fixed at 0.65 V/Ag-AgCl.

RESULTS AND DISCUSSION

Chemical and structural characterization of Co_RMn-LDH. From the literature, two methods of preparation were used to synthesize Co_RMn-LDH. Co_RMn-LDH powders were mainly prepared using the coprecipitation method at a fixed pH value of around 10. Most of these syntheses were conducted under oxidative conditions, either under air[35, 52] or dioxygen[53] , with added H_2O_2[31, 54] with the purpose of forcing the oxidation of Mn(II) to Mn(III) even Mn(IV). Coatings of Co_RMn-LDH thin films on scaffolders (i.e. Ni foam[55-56], carbon fibers[35], carbon cloth[57] or activated carbon[58]) were better obtained by the nucleation/crystal growth separation method using urea as base-retardant agent. Regarding XRD data, impurities were observed in many cases, while the purest reported Co_RMn-LDH phases display a poor crystallinity[31, 36-37, 54, 59]. So far no investigation was done on Co_RMn-LDH chemistry and structure while applications for such layered materials are emerging.

In the present study, the Co_RMn-LDH (R = 1, 2, 3, 4, 5) were synthesized by the coprecipitation method at a final pH of 10.0 at 50 °C, R corresponding to the initial Co/Mn molar ratio. The reaction was conducted under inert atmosphere (N_2), avoiding the presence of dioxygen, in order to limit, in a certain extent, the oxidation of the divalent metals and to insure the formation of pure LDH phases instead of cobalt or manganese oxides or oxohydroxides. Nevertheless, the centrifugation/washing step was conducted under air atmosphere, step during which partial oxidation of Co and Mn occurs through a topochemical reaction.

The chemical compositions of the five Co_RMn-LDH were determined by combining EDX and XPS data (Table 1). Both techniques confirm the presence of Co and Mn in the samples. The Co/Mn ratios, determined by EDX, are close to the metal ratios (R) used in the initial salt solutions, indicating that the synthesis conditions insure a total coprecipitation of both transition metals. The Co/Mn ratios determined by XPS are in good agreement with the EDX data, showing that all materials display a high chemical homogeneity from surface to bulk. However, as thickness analysis by XPS is less than 10 nm, i.e. statistically <20 nm for one platelet, XPS quantification concerns at the most only 40 % of the total atoms from bulk and surface effect can only be observed by this later technique.

The XRD patterns of Co_RMn-LDH are all consistent with the formation of LDH phases in major proportion (Figure 1A). Minor impurities are present in all cases, except for the compound with R = 3 which corresponds to the purest and best crystallized LDH structure. For the Mn-rich LDH phases (R = 1 & 2), the contamination by $MnCO_3$ (COD - 1548822) is observed while for the compounds with the lower contents of Mn (R = 4 & 5), hexagonal β-$Co(OH)_2$ (COD 1548810) is the only detected impurity. Le Bail whole pattern decomposition method was applied to determine the cell parameters, assuming a hexagonal unit cell with a rhombohedral space group R-3m as often reported for LDH systems (Figure S1). A slight decrease in the cell parameter ***a*** is observed for increasing values of Co/Mn ratio (Table 1) consistently with the increased amount of Co in the LDH structure as expected from the

difference in Co *vs* Mn ionic radii[60], but probably not in the expected proportion due to the presence of $MnCO_3$ and β-$Co(OH)_2$ phases. On the other hand, the interlayer distance is almost constant at around 7.60 Å, a value that is consistent with the presence of small anions, such as CO_3^{2-}, intercalated in between the layers.

Table 1. Chemical compositions and structural data of Co_RMn-LDH.

LDH	EDX	XPS		XRD			
R	Co/Mn	Co/Mn	M^{II}/M^{III}	a (Å)	c (Å)	d (Å)	Coherent domain L_{00l}/L_{110} (Å)
1	1.0	1.2	0.55	3.12012(5)	22.7560(4)	7.585	430/360
2	2.0	2.6	2.60	3.12282(5)	22.7985(5)	7.599	550/840
3	3.1	3.1	2.13	3.11450(2)	22.7748(1)	7.600	330/550
4	4.0	4.3	2.19	3.11357(7)	22.819(7)	7.606	340/350
5	5.2	5.1	4.01	3.1103(1)	22.799(1)	7.599	340/200

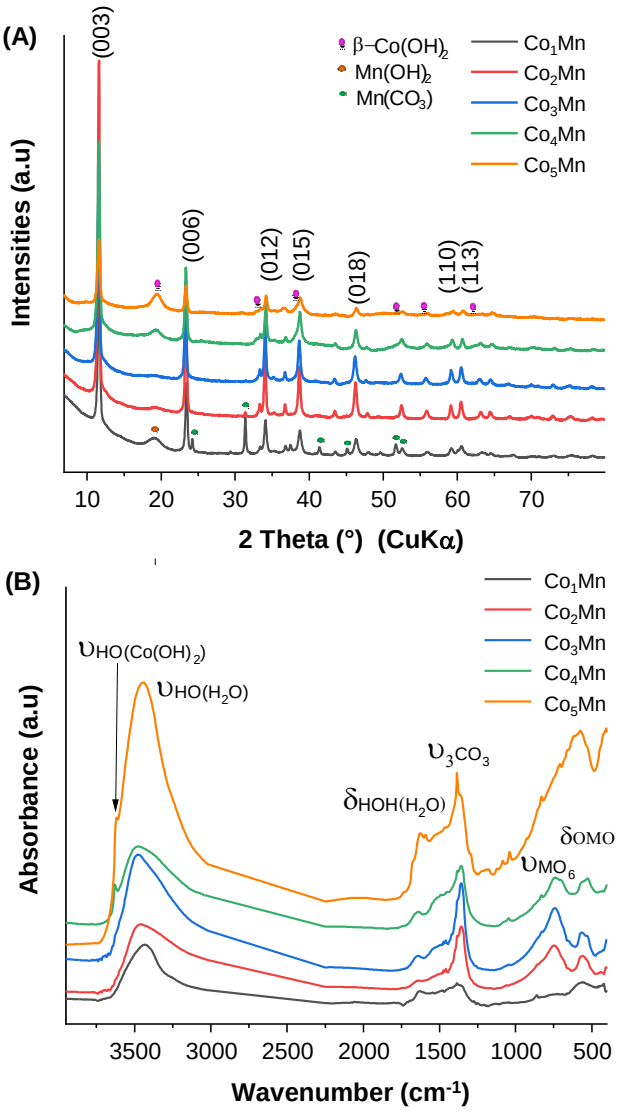

Figure 1. Powder X-ray diffraction patterns A) and FTIR B) of Co_RMn-LDH ($1 \leq R \leq 5$) series.

The FTIR spectra confirmed the intercalation of carbonate ($\nu_3(CO_3)$ = 1361 cm^{-1}, $\nu_2(CO_3)$ = 861 cm^{-1}, $\nu_4(CO_3)$ = 725 cm^{-1}) in the LDH structure (Figure 1B) and the presence of the above-mentioned minor impurities for Co_RMn compounds with $R \neq 3$ whose infrared characteristic bands display increased intensities (ν(OH) of $Co(OH)_2$ at 3629 cm^{-1} for R = 4, 5); ($\nu_2(CO_3)$ of $MnCO_3$ at 861 cm^{-1} for R = 1).

Representative SEM images of the Co_RMn-LDH compounds and TEM images of Co_3Mn-LDH are shown in Figure S2 and Figure S3. The Co_RMn-LDH solids (R = 2, 3, 4) display well identified, individual hexagonal platelets with an average width and thickness of about 200-580 nm and 40-60 nm, respectively. Co_RMn-LDH (R = 1, 5) samples display an inhomogeneity in terms of particle size that may be related to the presence of additional phases. High magnification (x104 K) of Co_3Mn-LDH TEM images (Figure S3) clearly indicates that large mosaic crystals are formed by a stacking of face-to-face oriented nano-slabs with a rather high number of edge atoms.

To gain further information on the chemical composition of the samples, XPS was used as a fine probe for the determination of the oxidation states of both Co and Mn. The presence of C, O,

Mn and Co elements is clearly seen on the survey spectrum of Co_3Mn-LDH (Figure S4). Mn2p and Co2p spectra display the typical two orbital spin-orbit doublets ($2p_{3/2}$ and $2p_{1/2}$) accompanied with shake-up satellites (Sat). The peak fittings of the well-defined Co2p and Mn2p peaks were done

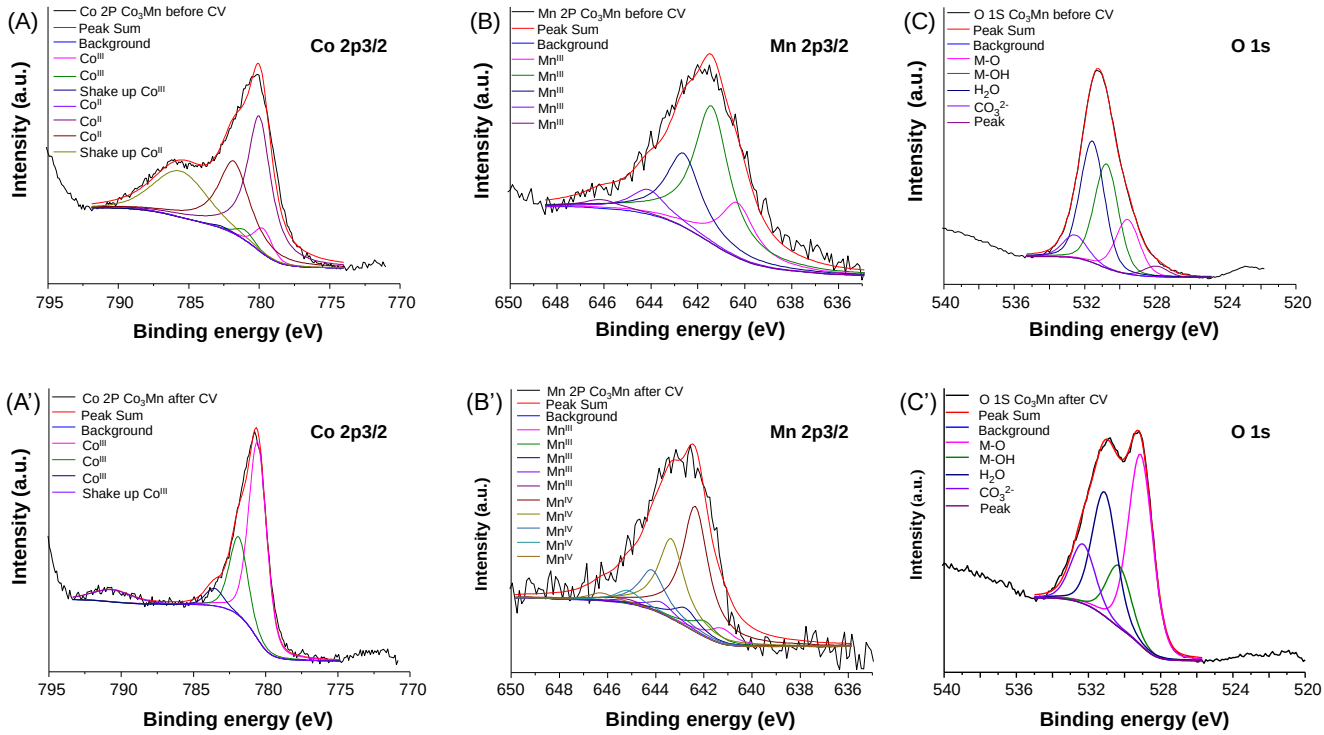

Figure 2. XPS spectra of Co_3Mn-LDH before and after electrochemical oxidation in 0.1 M NaOH, $Co2p_{3/2}$ (A, A'), $Mn2p_{3/2}$ (B, B'), O1s (C, C').

using parameters described in Refs[43, 61-63] involving sets of multiplets, justified by the high-spin configuration of Co and Mn in Co_RMn-LDH, as shown in Figure 2 for the $2p_{3/2}$ peaks. The peak energies (E_b) of the sets of multiplets are listed in Table S1 and show a very weak divergence (<1.5 eV) for a large variety of Co_RMn compositions, with R from 1 to 5. The peak decompositions of Co2p clearly highlight the coexistence of two oxidation states Co(II) and Co(III).

These two oxidation states can be recognized by their satellite peaks[42-43]. Indeed, Co(II)$2p_{3/2}$ contributions have an associated strong satellite peak around 786.3 eV, whereas the Co(III)$2p_{3/2}$ exhibits a weak satellite peak at 790.4 eV (Figure 2A). A very good accuracy in the decomposition of the Mn2p peak is more difficult to obtain due to the low energy shift between the sets of multiplets of the different oxidation states. . Moreover, the very low recorded signal of the Mn3s, due to the low amount of Mn atom in the various LDH materials, prevents from distinguishing oxidation degrees as is usually done. However, the decomposition of the Mn2p peak mainly shows a majority of Mn(III) regardless of the Co_RMn-LDH composition (Figure 2B).

The relative abundances (in percentages) of (II) and (III) oxidation states for each TM were calculated as a function of the sample composition (R) (Figure S5). First of all, it must be pointed out that due to the presence of impurities in the samples (*vide supra*) it is difficult to get a simple trends. However, we can conclude that i) a partial oxidation of TM occurred during the coprecipitation process under N_2 atmosphere at pH 10.0, ii) Co(II) is the major component in all samples, the percentage of Co(III) being very dependent on the R value, with the lower values (6-8 % for R= 2, 3, 5 and 19 % and 17 % for R = 1 and 4, respectively (Figure S5), iii) Mn(III) is the highest contribution in the Mn2p peak, accompanied by a low Mn(II) signal intensity in Co_RMn R =2, 4 and 5, iv) the total M(II)/M(III) ratio for Co_3Mn and Co_4Mn is nearly equal to 2.0 (Table 1).

The fit and the position of the O1s peak can give information about the nature of the phase and the presence of impurities. The O1s peak of the Co_3Mn-LDH (Figure 2C) spreads over a large

range of binding energy (525 eV – 535 eV) that shows the contribution of different oxygen species (Table S1 and Table 2). The component at 531.2 eV corresponds to oxygen from the Co_3Mn hydroxylated layers[43, 61].

Table 2. Relative abundance (%) of atomic species in each core level for Co_3Mn-LDH before and after electrochemical oxidation (0.1 M NaOH) determined by XPS.

Core level	Atomic species	Relative abundance (%)	
		Pristine	Oxidized
Co2p	Co(II)	90	-
	Co(III)	10	100
Mn2p	Mn(II)	-	-
	Mn(III)	100	-
	Mn(IV)	-	100
O1s	M-O	10	44
	M-OH	36	14
	H_2O	46	28
	CO_3^{2-}	11	14

This peak reveals also the presence of oxygen from the intercalated carbonate (533.1 eV) and oxygen from water molecules (532.2 eV)[61, 64] (Table S1). A small component, situated at lower binding energy (529.6 eV), can be attributed to the oxygen atoms involved in metal-oxide bonds.

This data confirms that the Co_3Mn compound is a pure LDH phase with only 10 % of metal oxide surface impurity (Table 2).

In order to confirm the oxidation state of both Co and Mn in the pristine and oxidized (after CV, *vide infra*) Co_3Mn phase, X-ray absorption spectra (XAS) were recorded at the Co (Figure 3A) and Mn K edges (Figure 3B) and compared with reference samples at different formal oxidation states.

On one hand, the energy position of the rising edge which is sensitive to the formal oxidation state of the absorbing atom[65], everything else being equal, is pointed at 7718.9 eV for the cobalt element in the pristine Co_3Mn phase (Figure 3A) which is an intermediate value between the CoO (-0.8 eV) and Co_3O4 (+1.1 eV) reference phases (Table 3).

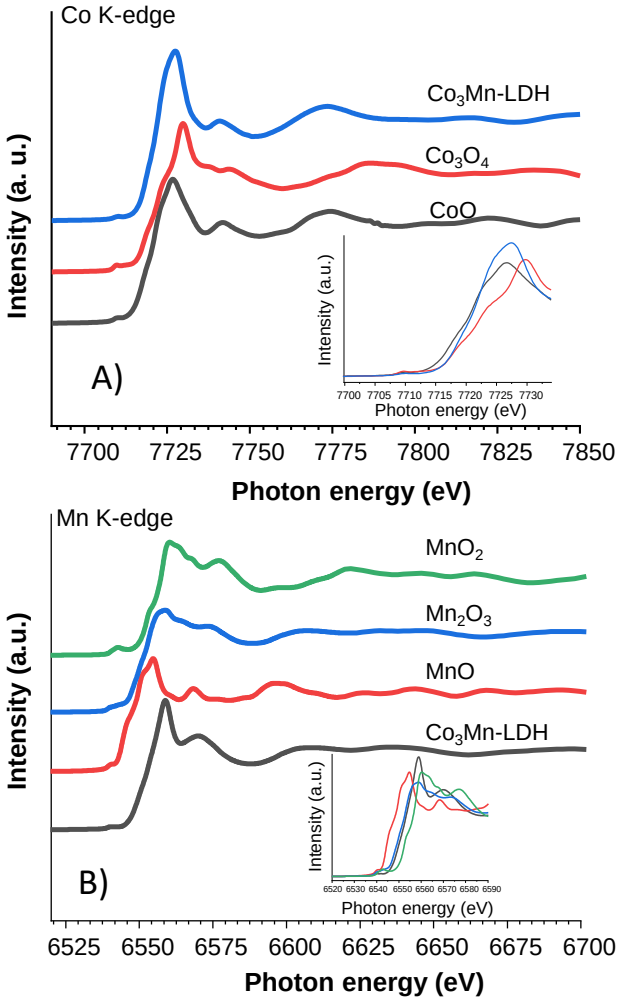

Figure 3. Co and Mn K-edge spectra of Co_3Mn-LDH and reference samples.

On the other hand, the absorption maximum corresponding to the allowed 1s → 4p transition is located at 7727.5 eV for the pristine LDH, a value slightly shifted at higher energy (+ 0.7 eV) than the one reported for pure Co(II) species such as CoO and at lower energy (-2.3 eV) compared to Co_3O_4 where Co is present at the formal oxidation state +2.66[66]. Taking into account those features together with the fact that similar XANES spectrum was obtained for $Co(II)_{0.85}Co(III)_{0.15}$ LDH by Vialat et al.[8], we assume the presence of a major contribution of Co(II) and a minor presence of Co(III) in good agreement with the XPS results. Partial oxidation of Co(II) is then confirmed. The valence of manganese can be discussed by comparison of the Mn absorption edge

with Mn(II)O, $Mn(III)_2O_3$ and $Mn(IV)O_2$ reference spectra (Figure 3B). With a rising edge position at 6550.3 eV, the Mn XANES spectrum is similar to that of Mn_2O_3 (6549.4 eV). That result clearly identifies a pure Mn(III) oxidation state in Co_3Mn-LDH (Table 3), confirming the XPS data. This tendency of LDH structure to stabilize the Mn(III) oxidation state when performing basic coprecipitation of Mn(II) salt was also observed for Ni-Mn-Fe[67] and Mg-Mn-Al LDH[68] by XAS studies.

Table 3. Co and Mn X-ray absorption energies of the rising edge for Co_3Mn before and after CV and reference samples. The tabulated values correspond to those for a normalized absorbance in the rising edge equal to 0.5.

Phases	Rising edge position (eV)	
	Co K-edge	Mn K-edge
Co_3Mn (pristine)	7718.9	6550.3
Co_3Mn (oxidized)	7721.2	6552.2
CoO	7718.1	-
Co_3O_4	7720.0	-
MnO	-	6544.7
Mn_2O_3	-	6549.4
MnO_2	-	6552.3

A TGA analysis was carried out to complete the detailed chemical characterization of the Co_RMn-LDH compounds. Differential thermogravimetry (DTG) plots of Co_RMn are reported in Figure S6A. The mechanism of thermal decomposition, dominated by dehydration processes (four events for Co_3Mn-CO_3 Figure S6A-Insert), appears quite similar for the other Co_RMn compounds if additional decompositions of impurities are considered. Calcination of Co_3Mn-LDH at 900 °C corresponds to a total mass loss of 27.55 % and ends in the formation of a pure spinel phase as shown by XRD (Figure S6B). The whole X-ray diffraction pattern matches a cubic Fd-3m cell typical of spinel system, very well, with a refined parameter *a* obtained from Le Bail refinement equal to 8.2082(1) Å. Interestingly for all Co_RMn phases, all TM cations are incorporated under calcination into a single spinel phase thanks to the flexibility of the oxidation states of both Co and Mn to fit the required $A(II)B(III)_2O_4$ spinel structure with variable chemical composition. Finally, it came out from the quantification of TGA weight losses that Co_3Mn-LDH chemical composition could be near $Co_{2.27}Mn_{0.73}(OH)_6(CO_3)_{0.48}.1.32H_2O$ formula.

Structural characterization of Co_3Mn-LDH. The Fourier transforms of the extended absorption fine structure signals (EXAFS) at both Co (Figures 4A) and Mn K-edges (Figure 4B) of Co_3Mn-LDH and Figure S7 exhibit two mains peaks resulting from the backscattered shells of the first and second neighbors.

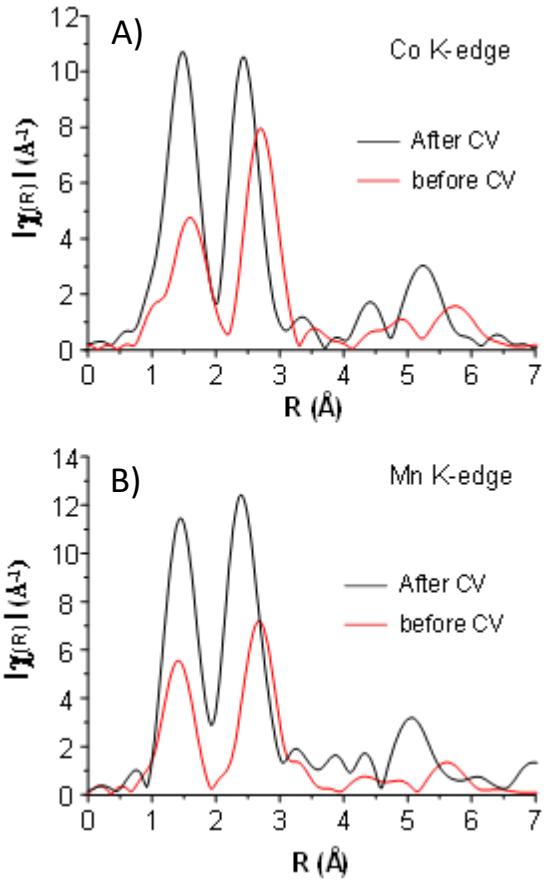

Figure 4. Fourier transforms of Co and Mn K-edge EXAFS signals of Co_3Mn before and after CV.

The first contributions appear in the 1 - 2 Å regions with a maximum at ~1.6 Å and at ~1.4 Å respectively for the Co and Mn spectra. It is due to the first shell scattering of the six oxygen neighbours (MO_6). Fitted metal-oxygen distances are reported in Table 4. Because of a smaller ion-

ic radius for Mn(III) than for Co(II), the Mn-O bond lengths (1.94 Å) are shorter than for Co-O (2.08 Å) (Table 4). The second peaks correspond to the first shell of metal, at (Co,Mn)-(Co,Mn) distances

Table 4. Atomic distances of Co_3Mn before and after CV from EXAFS analysis. $S_0^2 = 0.75$ (0.71) at the Co (Mn) K edge, Coordination numbers were fixed at 6 for both coordination shells at the r distances. DW parameters are the Debye-Waller factors. Fitting range: Δk: 3.5 -10.3 $Å^{-1}$ and ΔR: 1.0-3.2 Å.

Samples		Co-O	Mn-O	Co-(Co,Mn) (Co K-edge)	Mn-(Co,Mn) (Mn K-edge)
Co_3Mn (pristine)	r (Å)	2.08(1)	1.94(2)	3.13(1)	3.13(2)
	DW ($Å^2$)	0.0093(8)	0.0077(17)	0.0060(4)	0.0054(11)
Co_3Mn (oxidized)	r (Å)	1.91(1)	1.90(2)	2.85(1)	2.85(2)
	DW ($Å^2$)	0.0026(6)	0.0014(15)	0.0056(6)	0.0029(15)

similar for both elements (Table 4). As expected, only one M-M distance is obtained due to a unique crystal site for both Co and Mn.

Owing to the apparent purity and good crystallinity of Co_3Mn-LDH an in-depth structural investigation was performed.

The strong intensity of 01*l* (l = 2, 5, 8) reflections, observed on the XRD pattern (Figure 5), clearly indicates a staking sequence corresponding to the classic $3R_1$ polytype commonly encountered in the hydrotalcite supergroup.

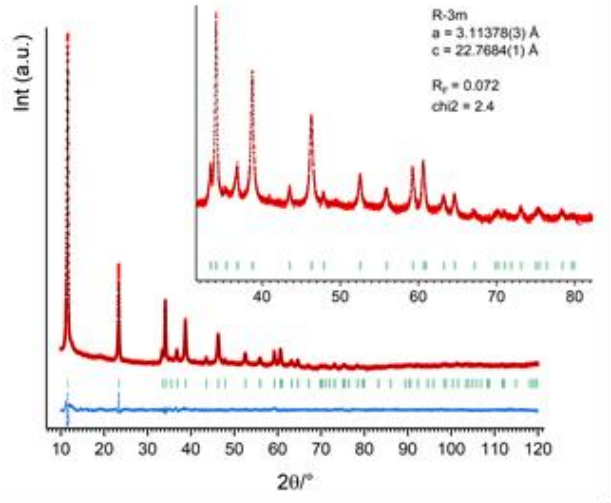

Figure 5. Rietveld refinement of the powder X-ray diffraction pattern of Co_3Mn-LDH: Experimental powder X-ray diffraction pattern (black-dots), calculated pattern (solid red line), Bragg reflections (green ticks), and difference profiles (blue dots, at the bottom).

Furthermore, the careful examination of the pattern confirms the absence of supercell reflections; therefore, a cation ordering within the hydroxide layer and/or an ordering of the interlayer species are unlikely.

As mentioned by Mills et al.[69], M^{2+}–M^{3+} ordering may not be detected by XRD if successive layers are offset in a disordered fashion. However, in the present case, the relative sharpness of the 01*l* and 113 reflections allow us to exclude the presence of stacking faults and turbostratic disorders.[70] On the other hand, a rather common alternative explanation is that the cation ordering cannot be observed due to similar atomic scattering factors, which could be applied here with Co and Mn.

To start the Rietveld structure refinement of Co_3Mn-LDH, we considered, as initial structural model, the single-crystal structure of hydrotalcite $Mg_6Al_2(OH)_{16}(CO_3)(H_2O)_4$ recently reported by Zhitova et al.[71], Co and Mn atoms were placed on the same site (3a) consistently with a disordered distribution of the cations within the hydroxide layers, with a Co/Mn molar ratio fixed to 3.1 as proposed by EDX and XPS analysis (Table 1). This leads to a single M(Co, Mn)–OH bond length first fixed to 2.044 Å in accordance with the mean distance that can be obtained from EXAFS data as follows : 2.08 * 0.756 + 1.94*0.243=2.044 Å.

In the model structure, the C atom of carbonate anions occupies the (6c) site lying directly

below the metal cations, and the oxygen atoms of carbonate anions and water molecules occupy a single set of sites (18g). We first assumed a similar distribution of the interlayer species, with starting occupancies derived from experimentally determined chemical composition i.e. $Co_{2.27}Mn_{0.73}(OH)_6(CO_3)_{0.48}.1.32\ H_2O$. The z coordinate of OH, the z coordinate of C and the x coordinate of O1 (oxygen atoms of CO_3 and H_2O) are the only three refinable atomic parameters in this model structure ; they were initially kept fixed so as to start refining with suitable M-OH and C-O distances respectively 2.044Å and 1.29Å.

At this stage of the refinement, the difference Fourier map was computed and indicated a maximum in the residual electron density observed at the position (0,0,0.5) and corresponding to the (3b) site. This site is the midpoint of the line joining the hydroxyl groups of adjacent metal hydroxide layers, hence suited for an occupation by water molecules with hydrogen bonding with the metal hydroxide layer.

Therefore, interlayer water molecules were included in this position as Ow atom and its occupancy was refined together with that of O1 and C under the constraint that their sum be close to the interlayer composition determined experimentally. Finally, the coordinates of OH, C and O1 atoms were refined. It was also possible to refine the isotropic atomic displacement parameters (Biso) of M and OH atoms in the layers while a fixed value of 3.0 $Å^2$ was set to interlayers species, taken from the literature.[71] The results of the refinement are reported in Tables S2 and S3. The fit is satisfactory with a featureless difference profile as can be seen in Figure 5. The structure is represented in Figure 6.

The chemical formula derived from this structure refinement is $Co_{2.27}Mn_{0.73}(OH)_6(CO_3)_{0.43}(OH)_{0.1.}1.56H_2O$ (M_w =328.56 $g.mol^{-1}$), very close to that determined experimentally. The site occupancy of C slightly lower than that expected (8 %) led us to consider the presence of a small amount of hydroxyl ions as charge compensating anion and located on O1 position; indeed, with a combination of both coulombic and H-bonding interactions, the 18g site is ideal for a mixed occupancy (Figure 6A). Given the high synthesis pH conditions used here, the presence of residual OH anion is not surprising. Moreover similar co-intercalation phenomena involving OH species have already been reported.[72-73]

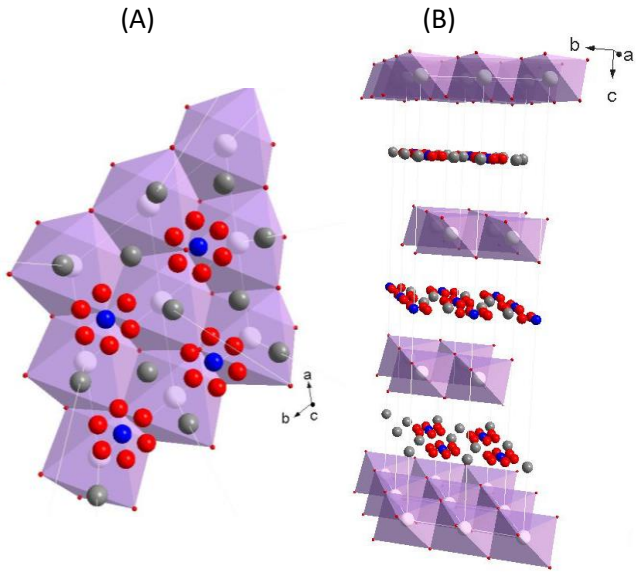

Figure 6. A) Arrangement in the interlayer space viewed along the c-axis with carbonate anions distributed on 6c sites (C atoms in grey) and 18g sites (O atoms in red), hydroxyl anions on 18g sites, and water molecules both on 18g and 3b sites (in blue), B) Structure of the Co_3Mn-LDH viewed along the a- axis.

Table S3 lists interatomic distances and angles. The refined M-OH 2.0410(7) Å and C-O 1.241(3) Å distances are consistent with EXAFS data and the presence of carbonate anions, respectively. The distortion of the $M(OH)_6$ octahedra with OH-M-OH angles significantly different from 90° leads to two OH-OH distances, an in-plane distance (measured perpendicular to the c-axis) at 3.11378(2) Å and an out-of-plane distance (shared octahedral edge) at 2.63982(2) Å These two distances are very different from those observed in $Mg_6Al_2(OH)_{16}(CO_3)(H_2O)_4$ (3.0728 Å and 2.6814 Å, respectively) indicating an important in-plane elongation of $M(OH)_6$ octahedra and a flattening of the hydroxide layer in Co_3Mn-LDH. These values are actually comparable to those reported for M-Ga-CO_3 LDH series with M = Ni,Co,Mn.[74] The comparison with $Co_4Ga_2(OH)_{12}CO_3.3H_2O$ sample is particularly

interesting first because of the presence of cobalt, secondly because the M^{2+}/M^{3+} ratio is equal to 2 like in Co_3Mn-LDH and finally because the ionic radius of Ga^{3+} (0.76 Å)[75] is close to that of Mn^{3+} (0.78Å). As shown by the authors of this previous study,[74] the strength of the coulombic attraction and hydrogen bonding between the layer and the interlayer can be reflected in M---CO_3/H_2O and OH---CO_3/H_2O distances, respectively. With M/Ga---CO_3/H_2O distances almost constant in M-Ga-CO_3 LDH series (3.97 ± 0.01 Å), it was established that the coulombic interaction is similar in all samples and independent of the M^{2+} cation. The Co/Mn---CO_3/H_2O distance obtained here i.e. 3.99293(2) Å allowed us to say that coulombic interaction may also be independent of the M^{3+} cation (Figure 6B). Furthermore, with a OH---CO_3/H_2O distance of 2.8208(9) Å, $Co_4Ga_2(OH)_{12}CO_3.3H_2O$ was found to display the strongest hydrogen bonding. A similar value is obtained here for Co/Mn---Ow i.e. 2.82807(2) Å therefore suggesting strong hydrogen bonding which could explain the remarkable stability of Co_3Mn-LDH phase.

All these characterizations converge to highlight a unique result, never reported so far. Many papers on Co_RMn-LDH have investigated a wide range of Co/Mn ratios but most of them have never reported, neither discussed their chemical compositions in terms of oxidation states. The structural refinement of the Co_3Mn-LDH shows a dense packing of the negatively charged interlayer species (OH^-, CO_3^{2-}) and water molecules. This is in favor of a continuous hydrogen-bonding network that electrostatically stabilizes the structure. Consequently, there is a lowering of the symmetry of the H-bonded CO_3^{2-} species that undergoes a distortion from a D3h to a C2v or even a Cs symmetry which accounts for a splitting of the ν_3 asymmetric stretching band into multiplet (1358, 1384, 1458, 1473, 1542 cm^{-1}).

Electrochemical behavior in 0.1 M NaOH. The electrochemical behavior of Co_RMn-LDH series was then evaluated using cyclic voltammetry (CV) in a three-electrode cell system. Cyclic voltammograms of Co_3Mn-LDH in 0.1 M NaOH are shown in Figure 7A. The first scan corresponds to an irreversible peak situated at ≅ 0.6 V/Ag-AgCl. The following cycles displayed a stable signal with a quasi-reversible redox signal at Ep_a = 0.320 V/Ag-AgCl and Ep_c = 0.110 V/Ag-AgCl, respectively.

The value of charge Q_a exchanged during the electrochemical oxidation can be estimated from the peak area measured in CV at low scan rate (v = 10 $mV.s^{-1}$). The charge (Q_a = $4x10^{-4}$ C) of the stable third cycle corresponds to 33% of the initial (Q_a $1.2x10^{-3}$ C of the first cycle). The current intensity, as well as the potential peak, depend on the Co content in the samples. The highest redox current was observed for Co_3Mn-LDH (Figure 7B). An optimum electroactivity was reported in the literature for a Co/Mn ratio of 2.[31, 35] This value is close to that found in the present work.

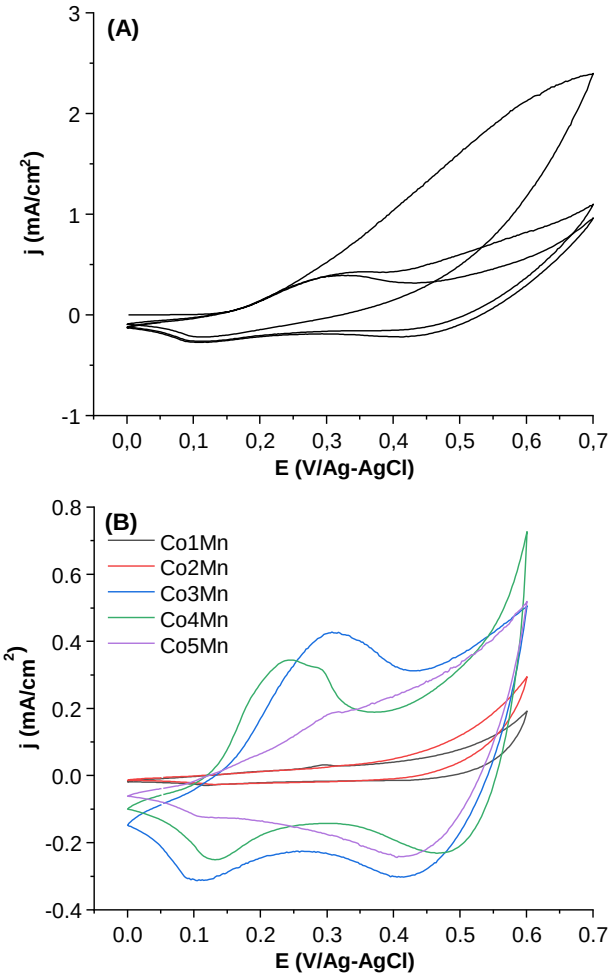

Figure 7. A) Three first cycles of Co_3Mn-LDH recorded in cyclic voltammetry. B) CV curves of

Co_RMn-LDH (third cycles) in 0.1 M NaOH, v = 10 mV s^{-1}.

Compounds with higher R ratio (R = 4 and 5) display a decrease in the electrochemical response with a new contribution at Ep_a = 0.29 V/Ag-AgCl, corresponding to β-$Co(OH)_2$ impurity.

The presence of Mn in the LDH structure seems to boost the electrochemical response of the cobalt-based LDH, in comparison with the electrochemical response obtained with β-$Co(OH)_2$ and CoAl-LDH[35].

To address the synergistic effect of the Co and Mn TM combination, the Co_3Mn-LDH modified electrodes were characterized before and after the electrochemical oxidation by EIS, SEM, EDX, XPS, XAS, DRX and FTIR. Figure 8 shows the SEM images of the Co_3Mn-LDH film before (A) and after (B) potential cycling (3 scans) in 0.1 M NaOH. Thanks to the synthesis conditions allowed us to prepare stable colloidal suspensions of Co_3Mn-LDH, the film coated on the electrode was highly homogeneous and dense with well-defined individual nearly monodisperse hexagonal platelets (Figure 8A).

After the electrochemical treatment, no noticeable change in the film morphology was observed (Figure 8B), highlighting the high stability of the Co_3Mn-LDH phase. The diffusion of an electroactive probe, $K_4Fe(CN)_6$, through the LDH thin film was analysed by CV using Randles−Sevcik relation at different scan rates ($10 < v < 100$ mVs^{-1}) (Figure S9A). In comparison to the bare PGE electrode, the peak current increases slightly and the signal remains reversible and governed by a diffusional process (ip_a fct $v^{1/2}$). This proves that the permeability of the LDH is good and that an apparent electroactive surface can be estimated as 27 % higher than the surface of the bare electrode.

The Co/Mn ratio in the oxidized film, determined by EDX and XPS, were 3.3 and 2.8, respectively. Therefore, no significant film destruction or metal leaching in the electrolyte solution was observed during the electrochemical treatment. The Nyquist plots of the EIS spectra of the pristine Co_3Mn-LDH at OCP_i and at fixed potential (0.3 V/Ag-AgCl), clearly show differences in the electrochemical properties before and after the electrochemical oxidation (Figure S9B). The pristine Co_3Mn-LDH electrode is characterized by a great depressed semicircle, whereas a well-defined loop was obtained for the oxidized film, which corresponds to a low value for the charge transfer resistance (~130 Ω). XPS analysis has shown a clear evolution of the experimental spectra in relation with the redox processes. Indeed, TM were oxidized to reach 100 % of Co(III) (Figure 2A') and 100 % of Mn(IV)(Figure 2B') in the oxidized sample (Table 2) which corresponds to an electron transfer of -0.92 e^-/TM leading to an average oxidation state of +3.8/TM atom). It is also interesting to note the splitting of the O1s peak after the electrochemical oxidation (Figure 2C'). In the oxidized Co_3Mn-LDH phase, the component situated at lower energy 530.0 eV, corresponding to the oxygen atoms involved in metal-oxide bonds, increases whereas the O1s in metal-hydroxides bonds situated at higher energy (E_b = 531.2 eV) decreases simultaneously [43, 61] (Table 2). Of course, these variations of oxidation states are determined for the extreme surface as determined by XPS.

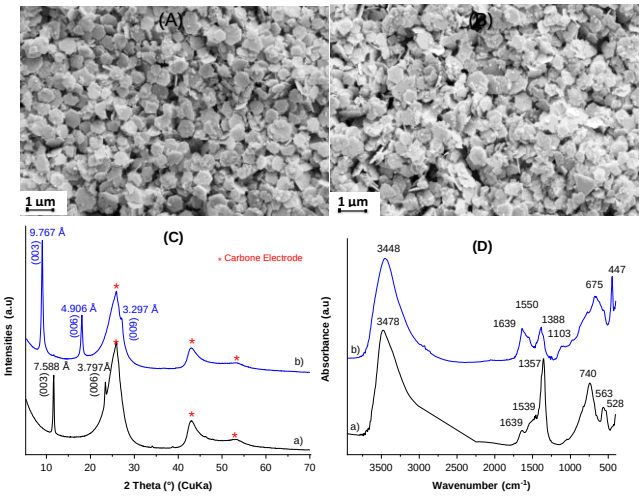

Figure 8. SEM images of the Co_3Mn-LDH film before (A) and after potential cycling (3 scans) in 0.1 M NaOH (B). XRD and FTIR corresponding data.

Moreover, XANES and EXAFS (Figure 4) analysis confirms the change in oxidation states

of both Co (Figure 9A) and Mn (Figure 9B). From the comparison of the rising edge energy position of oxidized Co_3Mn-LDH (after CV) with reference samples reported in Table 3, it appears clearly that electrochemical activation forces the Co(II) to oxidize into Co(III) and the Mn(III) to Mn(IV). It is noteworthy that thanks to the oxidation of both cations, the formation of a less distorted structure than the pristine LDH is observed in which irrespective to the cation, the metal-oxygen and metal-metal distances in the first and second coordination shells are equal to 1.90 Å and 2.85 Å, respectively (Table 4, Figure S8). Those distances are characteristic of the local order of Co(III) when located in the octahedral sites of the spinel Co_3O_4 structure and of Mn(IV) in MnO_2.

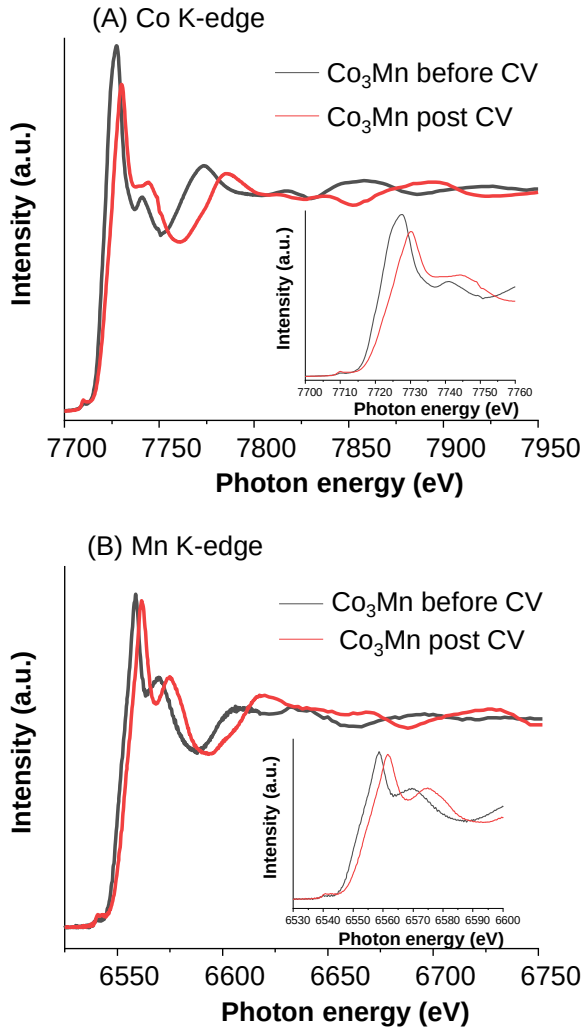

Figure 9. Co and Mn X-ray absorption spectra of Co_3Mn-LDH before and after oxidation in CV.

To gain further insight into the phase modification occurring during the oxidation process, the resulting oxidized Co_3Mn-LDH film coated on the carbon electrode was also characterized by XRD (Figure 8C) and FTIR (Figure 8D). Structural changes are clearly observed. The XRD of Co_3Mn-LDH thin films displays, beside the broad peak of the carbon electrode, the (00l) diffraction line series with high intensities due to a preferred orientation of the particles on the substrate. The three (00l) peaks of the oxidized Co_3Mn-LDH film shift toward the low 2theta angle values. This indicates an expansion of the interlayer domain from 7.588 Å (Table 1) to 9.767 Å, i.e. +2.179 Å, which is significantly higher than what has been previously observed with *operando* XRD measurement of oxidized CoAl-LDH films[76].

This expansion is accompanied by a structural change of both the layer and interlayer domains as shown by the comparison of the FTIR spectra and the occurrence of Na^+ cations identified by the XPS analysis (Figure S4) and the EDX analysis (data not shown). A part of the carbonate anions (ν = 1388 cm^{-1}) are expelled from the interlayer gallery simultaneously to an increase in the intercalated H_2O content (δ = 1639 cm^{-1}). Meanwhile the LDH layer seems to undergo a partial de-hydroxylation, as indicated by the decrease in the intensity of the ν (MOH) band (740 cm^{-1}) and the loss of the characteristic ν ($M(OH)_6$) (563 and 528 cm^{-1}) and δ(OMO) (400 cm^{-1}) bands.

Obviously the oxidation reaction of Co(II) and Mn(III) is assisted by a deprotonation and by the insertion of hydrated Na^+ cations inside the Co_3Mn-LDH and concerns the entire structure.

Electrocatalytic oxidation of H_2O_2. The electrocatalytic properties of Co_RMn-LDH as regard to H_2O_2 oxidation were evaluated using CV in Tris buffer solution pH 7.0 (anodic sweep between 0 and 0.9 V/Ag-AgCl, Figure 10) and reduction (cathodic sweep between 0 and -0.9 V/Ag-AgCl, Figure S10) and then compared to that obtained at the bare PGE.

As depicted in Figure 10A, the electrochemical response in neutral pH electrolyte is low for all the samples. However, upon addition of 5 mM H_2O_2, the Co_RMn-LDH modified electrodes exhibited significant oxidation (Figure 10B) and reduction (Figure S10) currents, in comparison with that observed at the bare electrode. Interestingly in both cases, the shape of the voltammogram curves and the peak intensities varied with the Co/Mn ratio. In oxidation, a hysteresis phenomenon was observed for the samples corresponding to a low Co amount in the LDH structure (R =1 and 2), whereas direct oxidation peaks were observed for the other samples. The highest catalytic current was obtained with the Co_3Mn-LDH which gradually increased with the H_2O_2 concentration (Figure 11A).

In reduction, the opposite was observed since the hysteresis phenomenon occurred with the samples having the highest Co/Mn ratio (R = 4 and 5) (Figure S10). The highest catalytic current in reduction was observed for the Co_1Mn-LDH. This confirms that Co_RMn-LDHs have electrocatalytic properties in the presence of H_2O_2 but the mechanism depends on the respective contribution of both metals in different electroactive sites. Indeed, as reported by Kuo et al. for mixed-valence CoMn oxides[77], the presence of multivalent species, i.e. Co(II)/Co(III) and Mn(III)/Mn(IV), contributes to the electrocatalytic performance in H_2O_2 reduction. Similarly, Su et al.[78] have shown that nanostructured cobalt oxides, photochemically synthesized, exhibit an electrocatalytic activity in both H_2O_2 oxidation and reduction. In both cases, the electrocatalytic performance seems to be highly associated with the formation of hierarchical nanostructures with a specific elemental composition. In the present study, the segregation-free multiple mixed-valence systems of Co(II)/Co(III) and Mn(III)/Mn(IV) with an optimum Co/Mn ratio (R =3) in the LDH structure may contribute to the high electrocatalytic performance. Based on the mechanisms proposed for the electrocatalytic oxidation of H_2O_2 by mixed valent oxides[79-80], we can postulate the following mechanism:

$$Co^{II}{}_xCo^{III}Mn_y{}^{III}\text{-LDH} + (x+y)OH^- \rightarrow Co^{III}{}_{1+x}Mn^{IV}{}_y\text{-LDH} + (x+y)e^-$$

$$Co^{III}{}_{1+x}Mn^{IV}{}_y\text{-LDH} + H_2O_2 \rightarrow Co^{II}xCo^{III}Mn_y{}^{III}\text{-LDH} + O_2 + H_2O$$

However, the presence of MnO_2 as a by-product in Co_1Mn-LDH induced an enhancement of the reduction activity but not in the oxidation. The same behaviour was reported with a MnO_2NPs/MgAl-LDH nanocomposite[21]. The hysteresis phenomenon suggests that H_2O_2 oxidation becomes easier when the Co_RMn-LDH films (R = 1 and 2) were electrochemically oxidized.

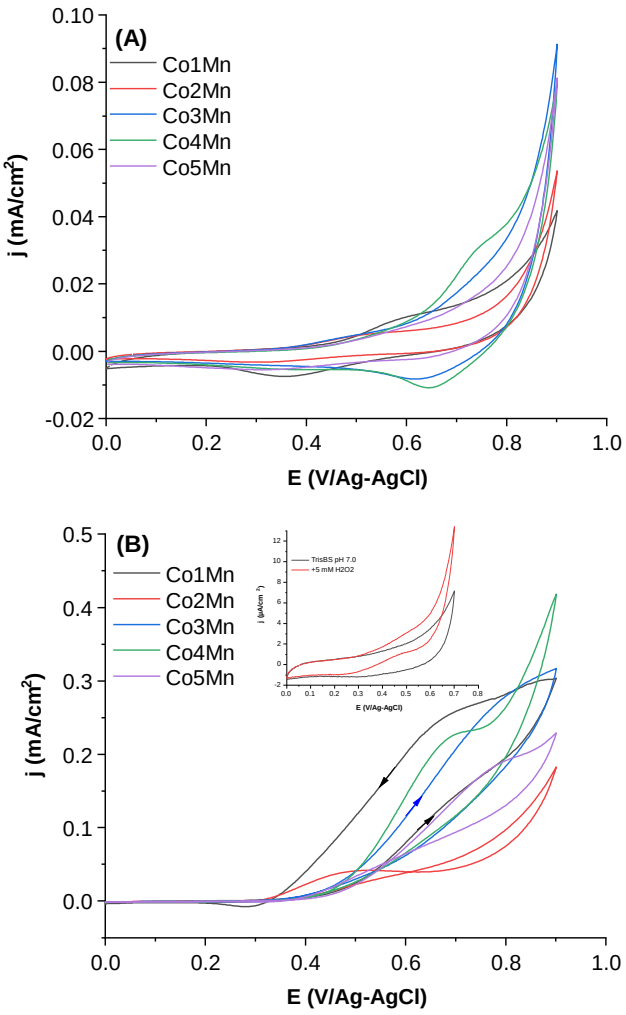

Figure 10. Cyclic voltammograms of the Co_RMn-LDH modified electrodes ($1 \leq R \leq 5$) (anodic sweep) in 0.1 M Tris buffer solution (pH 7.0) (A) in absence and (B) presence of 5 mM H_2O_2. Inset shows the CV curves under the same conditions using a bare PGE. (v = 10 mV s^{-1}).

The calibration curves of H_2O_2 were then established for Co_3Mn-LDH using chronoamperometry under stirring conditions at 0.65V/Ag-AgCl (Figure 11B). The influence of the amount of deposited catalyst and hence the thickness of the LDH film on the sensor response was examined. The reproducibility of the sensors was tested for three different electrodes for each amount of catalyst. The sensor response increased by doubling the amount from 10 to 20 µg with a good reproducibility, but for a thicker film (40 µg) the response became less reproducible and no significant enhancement of the amperometric response was observed. This confirms that Co_3Mn-LDH is effectively an electrocatalyst for H_2O_2 oxidation but an increase in the film thickness may limit the diffusion pathway of H_2O_2.

As shown in Figure11C, addition of 1 mM H_2O_2 caused an increase in the anodic current, with a response time (t_{95}) of 3 sec, and the presence of interfering species caused no current change except with ascorbic acid (21%). The linear range of the calibration curves was fixed according to the best correlation coefficient (R^2) (Figure 11D).

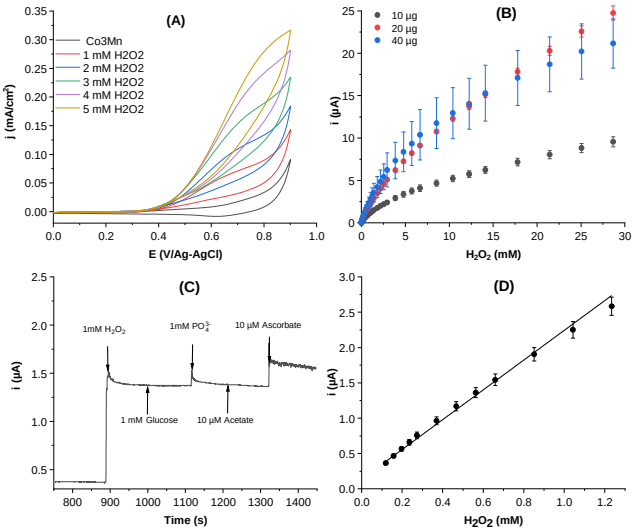

Figure 11. A) Cyclic voltammograms (anodic sweep) of the Co_3Mn-LDH modified electrode (20 µg) as a function of H_2O_2 concentration in the range from 1 to 5 mM (0.1 M pH 7.0 Tris buffer solution, *v* = 10 mV s-1), B) H_2O_2 calibration curve established using chronoamperometry at 0.65 V for 10 and 20, 40 µg of electrocatalyst, C) Current response as function of time of the sensor in the presence of 1 mM H_2O_2, glucose, phosphate and ascorbate, D) Linear range for H_2O_2 determination.

A linear response, satisfying Y= 0.13596(±0.015) + 2.10717(±0.050)x (R^2 = 0.994, n = 12), was obtained between 0.11 and 1.2 mM for 20 µg of Co_3Mn-LDH (Figure 11D). The sensitivity, calculated from the slope of this equation, was 30±0.7 mA M^{-1} cm^{-2} and the limit of detection (LoD) was 86 µM (S/N = 3). These values can be compared to those reported for sensors based on other LDH or mixed spinel oxides (Table 5), showing the interest of bifunctional CoMn-LDH in sensing H_2O_2 in neutral pH under oxidation condition leading to dioxygen generation. To a certain extent, depending on the envisaged application, our study shows that the use of expensive AuNPs can be omitted for the detection of H_2O_2 by using an oxidation process in neutral pH.

Table 5. Detection of H_2O_2 by electrochemical oxidation using LDH modified electrodes

LDH	Sensing conditions	Sensitivity (mA M^{-1} cm^{-2})	LoD (M)	Ref
NiAl-NO_3	E_{app} = 0.06V pH 13	-	$9x10^{-9}$	26
CoAl-NO_3	E_{app} = 0.49 V pH 13	-	$5x10^{-8}$	26
NiFe-NO_3	E_{app} = 0.4 V pH 13	1704	$5x10^{-7}$	27
Co_3Mn-CO_3	E_{app} = 0.65 V pH 7	30	$8.6x10^{-5}$	This work
Hybrids				
CoAl/Fe TSPP	$E_{app} \cong$ 0.5 V pH 13	-	$1.8x10^{-8}$	28
CoAl/N GB	E_{app} = 0.38 V pH 13	-	$9x10^{-7}$	29
Nanocomposites				
MWCNTs/CoAl-CO_3	E_{app} = 0.23 V pH 14	118	$5x10^{-6}$	30
Au_{NPs}/C		60	$1x10^{-7}$	

oAl-CO_3				
Au_{NPs}/MgMn-CO_3	E_{app} = 0.55 V pH 7	23	$2.5x10^{-7}$	37
Au_{NPs}/CoMn-CO_3		125	$6x10^{-8}$	

CONCLUSIONS

In this study, we have demonstrated the electrocatalytic performance of a novel Co_RMn-LDH material for the electrocatalytic detection of hydrogen peroxide, a key molecule in many chemical and biochemical pathways. This new sensor is effective in neutral pH compared to those reported in the literature. This distinctive property arises from a unique divalent/trivalent transition metal composition leading to a synergistic electronic coupling between mixed-valent Co(II)/Co(III) and Mn(III) cations, hosted jointly in the octahedral sites of the layered double hydroxide structure. Indeed, precipitation of Co(II) and Mn(II) under O_2-free and basic conditions allows for a self-adjustment of the Co and Mn oxidation states giving rise to a unique LDH phase with the presence of Co(II)/Co(III) and Mn(III) cations. In-depth structural refinement revealed the formation of a unique $Co_{2.27}Mn_{0.73}(OH)_6(CO_3)_{0.43}(OH)_{0.1.}1.56$ H_2O LDH phase stabilized with co-intercalated CO_3^{2-} and OH^- anions and water molecules. Chemical compositions and structure were supported by in depth XPS and XAS analysis.

These new results highlight, once more, the great flexibility and ability of the LDH structure to accommodate a large panel of transition metal compositions. This enhances the interest to further explore the chemistry of LDH for sustainable development. Combined with the biocompatibility of LDH for enzyme immobilization[18], the electrocatalytic behavior of these materials may be useful to explore new biosensor design.

ASSOCIATED CONTENT

Supporting Information

Detailed XPS data : fitted positions of Co, Mn, O in various materials, Co, Mn relative abundances; refined XRD patterns, atomic positions, bond angles and distances for Co3Mn LDH; electronic microscopy images and thermogravimetric analysis; EXAFS data; electrochemical and impedance measurements (CoRMn-LDH_JPhysChem C_SI.pdf).

AUTHOR INFORMATION

Corresponding Authors

* Claude Forano

E-mail: claude.forano@uca.fr

Université Clermont Auvergne, CNRS, SIGMA Clermont, Institut de Chimie de Clermont-Ferrand, F-63000 Clermont–Ferrand, France. ORCID :0000-0002-5522-6213

* Christine Mousty

E-mail: christine.mousty@uca.fr

Université Clermont Auvergne, CNRS, SIGMA Clermont, Institut de Chimie de Clermont-Ferrand, F-63000 Clermont–Ferrand, France. ORCID: 0000-0002-3003-2092

ACKNOWLEDGEMENTS

The authors are grateful to the selection committee of SOLEIL Synchroton (France) for supporting our project (proposal number 20190617) and to the local staff members on Rock beam line for technical assistance. This work was supported by a public grant overseen by the French National Research Agency (ANR) as a part of the "Investissements d'Avenir" program (ref: ANR-10-EQPX-45).

Dr. V. Prevot is acknowledged for her valuable experimental assistance for TEM image acquisition.

REFERENCES

1. Mousty, C.; Leroux, F., LDHs as Electrode Materials for Electrochemical Detection and Energy

Storage: Supercapacitor, Battery and (Bio)-Sensor. *Recent Pat. Nanotechnol.* **2012,** *6* (3), 174-192.
2. Asif, M.; Aziz, A.; Azeem, M.; Wang, Z.; Ashraf, G.; Xiao, F.; Chen, X.; Liu, H., A review on electrochemical biosensing platform based on layered double hydroxides for small molecule biomarkers determination. *Adv. Colloid Interface Sci.* **2018,** *262*, 21-38.
3. Baig, N.; Sajid, M., Applications of layered double hydroxides based electrochemical sensors for determination of environmental pollutants: A review. *Trends Env. Anal. Chem.* **2017,** *16*, 1-15.
4. Long, X.; Wang, Z.; Xiao, S.; An, Y.; Yang, S., Transition metal based layered double hydroxides tailored for energy conversion and storage. *Mater. Today* **2016,** *19* (4), 213-226.
5. Shao, M. F.; Zhang, R. K.; Li, Z. H.; Wei, M.; Evans, D. G.; Duan, X., Layered double hydroxides toward electrochemical energy storage and conversion: design, synthesis and applications. *Chem. Comm.* **2015,** *51* (88), 15880-15893.
6. Patel, R.; Park, J. T.; Patel, M.; Dash, J. K.; Gowd, E. B.; Karpoormath, R.; Mishra, A.; Kwak, J.; Kim, J. H., Transition-metal-based layered double hydroxides tailored for energy conversion and storage. *J. Mater. Chem. A* **2018,** *6* (1), 12-29.
7. Chen, H.; Hu, L.; Chen, M.; Yan, Y.; Wu, L., Nickel–Cobalt Layered Double Hydroxide Nanosheets for High-performance Supercapacitor Electrode Materials. *Adv. Funct. Mater.* **2014,** *24*, 934-942.
8. Vialat, P.; Mousty, C.; Taviot-Gueho, C.; Renaudin, G.; Martinez, H.; Dupin, J.-C.; Elkaim, E.; Leroux, F., High-Performing Monometallic Cobalt Layered Double Hydroxide Supercapacitor with Defined Local Structure. *Adv. Funct. Mater.* **2014,** *24* (30), 4831-4842.
9. Chitravathi, S.; Kumar, S.; Munichandraiah, N., NiFe-layered double hydroxides: a bifunctional O2 electrode catalyst for non-aqueous Li–O2 batteries. *RSC Adv.* **2016,** *6* (105), 103106-103115.
10. Wang, Y.; Yan, D.; El Hankari, S.; Zou, Y.; Wang, S., Recent Progress on Layered Double Hydroxides and Their Derivatives for Electrocatalytic Water Splitting. *Adv. Sci.* **2018,** *5* (8), 1800064.
11. Anantharaj, S.; Karthick, K.; Kundu, S., Evolution of layered double hydroxides (LDH) as high performance water oxidation electrocatalysts: A review with insights on structure, activity and mechanism. *Mater Today Energy* **2017,** *6*, 1-26.
12. Yan, K.; Wu, G.; Jin, W., Recent Advances in the Synthesis of Layered, Double-Hydroxide-Based Materials and Their Applications in Hydrogen and Oxygen Evolution. *Energy Technol.* **2016,** *4* (3), 354-368.
13. Cai, Z.; Bu, X.; Wang, P.; Ho, J. C.; Yang, J.; Wang, X., Recent advances in layered double hydroxide electrocatalysts for the oxygen evolution reaction. *J. Mater. Chem. A* **2019,** *7* (10), 5069-5089.
14. Li, K.; Guo, D.; Kang, J.; Wei, B.; Zhang, X.; Chen, Y., Hierarchical Hollow Spheres Assembled with Ultrathin CoMn Double Hydroxide Nanosheets as Trifunctional Electrocatalyst for Overall Water Splitting and Zn Air Battery. *ACS Sustainable Chem. Eng.*, **2018,** *6*, 14641-14651.
15. Tonelli, D.; Scavetta, E.; Giorgetti, M., Layered-double-hydroxide-modified electrodes: electroanalytical applications. *Anal. Bioanal. Chem.* **2013,** *405* (2-3), 603-614.
16. Lin, S.; Guo, X.; Qin, K.; Feng, L.; Zhang, Y.; Tang, Y., Efficient Production of Biomass-Derived C4 Chiral Synthons in Aqueous Solution. *ChemCatChem* **2017,** *9* (22), 4179-4184.
17. Mousty, C., Biosensing applications of clay-modified electrodes: A review. *Anal. Bioanal. Chem.* **2010,** *396* (1), 315-325.
18. Mousty, C.; Prevot, V., Hybrid and biohybrid layered double hydroxides for electrochemical analysis. *Anal. Bioanal. Chem.* **2013,** *405* (11), 3513-3523.
19. Asif, M.; Haitao, W.; Shuang, D.; Aziz, A.; Zhang, G.; Xiao, F.; Liu, H., Metal oxide intercalated layered double hydroxide nanosphere: With enhanced electrocatalyic activity towards H2O2 for biological applications. *Sens. Actuator B-Chem.* **2017,** *239*, 243-252.
20. Asif, M.; Liu, H.; Aziz, A.; Wang, H.; Wang, Z.; Ajmal, M.; Xiao, F.; Liu, H., Core-shell iron oxide-layered double hydroxide: High electrochemical sensing performance of H2O2 biomarker in live cancer cells with plasma therapeutics. *Biosens. Bioelectron.* **2017,** *97*, 352-359.
21. Asif, M.; Aziz, A.; Dao, A. Q.; Hakeem, A.; Wang, H.; Dong, S.; Zhang, G.; Xiao, F.; Liu, H., Real-time tracking of hydrogen peroxide secreted by live cells using MnO2 nanoparticles intercalated layered doubled hydroxide nanohybrids. *Anal. Chim. Acta* **2015,** *898*, 34-41.
22. Burek, B. O.; Bormann, S.; Hollmann, F.; Bloh, J. Z.; Holtmann, D., Hydrogen peroxide driven biocatalysis. *Green Chem.* **2019,** *21* (12), 3232-3249.
23. Chen, W.; Cai, S.; Ren, Q.-Q.; Wen, W.; Zhao, Y.-D., Recent advances in electrochemical sensing for hydrogen peroxide: a review. *Analyst* **2012,** *137* (1), 49-58.
24. Taviot-Guého, C.; Prévot, V.; Forano, C.; Renaudin, G.; Mousty, C.; Leroux, F., Tailoring Hybrid Layered Double Hydroxides for the Development of Innovative Applications. *Adv. Funct. Mater.* **2018,** *28* (27), 1703868.
25. Aziz, A.; Asif, M.; Ashraf, G.; Azeem, M.; Majeed, I.; Ajmal, M.; Wang, J.; Liu, H. J. M. A., Advancements in electrochemical sensing of hydrogen peroxide, glucose and dopamine by using 2D nanoarchitectures of layered double hydroxides or metal dichalcogenides. A review. *Microchim. Acta* **2019,** *186*, 671.
26. Yin, Z. J.; Wu, J. J.; Yang, Z. S., Amperometric sensors based on Ni/Al and Co/Al layered double hydroxides modified electrode and their application for hydrogen peroxide detection. *Biosens. Bioelectron.* **2011,** *26* (5), 1970-1974.

27. Tao, Y.; Chang, Q.; Liu, Q.; Yang, G.; Guan, H.; Chen, G.; Dong, C., Highly sensitive nonenzymatic H2O2 sensor based on NiFe-layered double hydroxides nanosheets grown on Ni foam. *Surf. Interfaces* **2018,** *12*, 102-107.
28. Shao, M.; Han, J.; Shi, W.; Wei, M.; Duan, X., Layer-by-layer assembly of porphyrin/layered double hydroxide ultrathin film and its electrocatalytic behavior for H2O2. *Electrochem. Commun.* **2010,** *12* (8), 1077-1080.
29. Kong, X.; Zhao, J.; Han, J. B.; Zhang, D. Y.; Wei, M.; Duan, X., Fabrication of Naphthol green B/layered double hydroxide nanosheets ultrathin film and its application in electrocatalysis. *Electrochim. Acta* **2011,** *56* (3), 1123-1129.
30. Heli, H.; Pishahang, J.; Amiri, H. B., Synthesis of hexagonal CoAl-layered double hydroxide nanoshales/carbon nanotubes composite for the non-enzymatic detection of hydrogen peroxide. *J. Electroanal. Chem.* **2016,** *768*, 134-144.
31. Song, F.; Hu, X. L., Ultrathin Cobalt-Manganese Layered Double Hydroxide Is an Efficient Oxygen Evolution Catalyst. *J. Am. Chem. Soc.* **2014,** *136* (47), 16481-16484.
32. Yi, Z.; Ye, C.; Zhang, M.; Lu, Y.; Liu, Y.; Zhang, L.; Yan, K., One-pot synthesis of etched CoMn-layered double hydroxides efficient for oxygen evolution reaction. *Appl. Surf. Sci.* **2019,** *480*, 256-261.
33. Wang, K.; Zhang, L.; Su, Y.; Shao, D.; Zeng, S.; Wang, W., Photoreduction of carbon dioxide of atmospheric concentration to methane with water over CoAl-layered double hydroxide nanosheets. *J. Mater. Chem. A* **2018,** *6* (18), 8366-8373.
34. Jagadale, A. D.; Guan, G.; Li, X.; Du, X.; Ma, X.; Hao, X.; Abudula, A., Ultrathin nanoflakes of cobalt-manganese layered double hydroxide with high reversibility for asymmetric supercapacitor. *J. Power Sources* **2016,** *306*, 526-534.
35. Zhao, J.; Chen, J.; Xu, S.; Shao, M.; Yan, D.; Wei, M.; Evans, D. G.; Duan, X., CoMn-layered double hydroxide nanowalls supported on carbon fibers for high-performance flexible energy storage devices. *J. Mater. Chem. A* **2013,** *1* (31), 8836-8843.
36. Li, M.; Cheng, J. P.; Wang, J.; Liu, F.; Zhang, X. B., The growth of nickel-manganese and cobalt-manganese layered double hydroxides on reduced graphene oxide for supercapacitor. *Electrochim. Acta* **2016,** *206*, 108-115.
37. Xu, L.; Lian, M.; Chen, X.; Lu, Y.; Yang, W., Amperometric sensing of hydrogen peroxide via an ITO electrode modified with gold nanoparticles electrodeposited on a CoMn-layered double hydroxide. *Microchim. Acta* **2017,** *184* (10), 3989-3996.
38. Rodríguez-Carvajal, J., Recent developments of the program FullProf. *Newsletter of the Commission for Powder Diffraction of the IUCr* **2001,** *26*, 12-19.
39. Thompson, P.; Cox, D. E.; Hastings, J. B., Rietveld refinement of Debye-Scherrer synchrotron X-ray data from Al2O3. *J. Appl. Crystallogr.* **1987,** *20*, 79-83.
40. Jarvinen, M., Application of symmetrized harmonics expansion to correction of the preferred orientation effect. *J. Appl. Crystallogr.* **1993,** *26*, 525-531.
41. Zhou, J.; Min, M.; Liu, Y.; Tang, J.; Tang, W., Layered assembly of NiMn-layered double hydroxide on graphene oxide for enhanced non-enzymatic sugars and hydrogen peroxide detection. *Sens. Actuator B-Chem.* **2018,** *260*, 408-417.
42. Koza, J. A.; Hull, C. M.; Liu, Y.-C.; Switzer, J. A., Deposition of β-Co(OH)2 Films by Electrochemical Reduction of Tris(ethylenediamine)cobalt(III) in Alkaline Solution. *Chem. Mater.* **2013,** *25* (9), 1922-1926.
43. Yang, J.; Liu, H.; Martens, W. N.; Frost, R. L., Synthesis and Characterization of Cobalt Hydroxide, Cobalt Oxyhydroxide, and Cobalt Oxide Nanodiscs. *J. Phys. Chem. C* **2010,** *114* (1), 111-119.
44. Jablonski, A., Evaluation of procedures for overlayer thickness determination from XPS intensities. *Surf. Sci.* **2019,** *688*, 14-24.
45. Mahjoub, M. A.; Monier, G.; Robert-Goumet, C.; Bideux, L.; Gruzza, B., New method for the determination of the correction function of a hemisperical electron analyser based on elastic electron images. *J. Electron Spectrosc. Relat. Phenom.* **2014,** *197*, 80-87.
46. Briois, V.; La Fontaine, C.; Belin, S.; Barthe, L.; Moreno, T.; Pinty, V.; Carcy, A.; Girardot, R.; Fonda, E., ROCK: the new Quick-EXAFS beamline at SOLEIL. *J. Phys. Conf. Ser.* **2016,** *712*, 012149.
47. Fontaine, C.; Belin, S.; Barthe, L.; Roudenko, O.; Briois, V., ROCK: A Beamline Tailored for Catalysis and Energy-Related Materials from ms Time Resolution to µm Spatial Resolution. *Synchrotron Radiation News* **2020,** *33*, 20-25.
48. Lesage, C.; Devers, E.; Legens, C.; Fernandes, G.; Roudenko, O.; Briois, V., High pressure cell for edge jumping X-ray absorption spectroscopy: Applications to industrial liquid sulfidation of hydrotreatment catalysts. *Catal. Today* **2019,** *336*, 63-73.
49. Newville, M., IFEFFIT : interactive XAFS analysis and FEFF fitting. *J. Synchrotron Rad.* **2001,** *8* (2), 322-324.
50. Ravel, B.; Newville, M., ATHENA, ARTEMIS, HEPHAESTUS: data analysis for X-ray absorption spectroscopy using IFEFFIT. *J. Synchrotron Rad.* **2005,** *12* (4), 537-541.
51. Vialat, P.; Leroux, F.; Taviot-Gueho, C.; Villemure, G.; Mousty, C., Insights into the electrochemistry of (CoxNi(1−x))2Al–NO3 Layered Double Hydroxides. *Electrochim. Acta* **2013,** *107* (0), 599-610.
52. Liao, P.; Zhang, C.; Zhang, L.; Yang, Y.; Zhong, L.; Wang, H.; Sun, Y., Higher alcohol synthesis via syngas over CoMn catalysts derived from hydrotalcite-like precursors. *Catal. Today* **2018,** *311*, 56-64.
53. Jia, G.; Hu, Y.; Qian, Q.; Yao, Y.; Zhang, S.; Li, Z.; Zou, Z., Formation of Hierarchical Structure Composed of (Co/Ni)Mn-LDH Nanosheets on MWCNT Backbones

for Efficient Electrocatalytic Water Oxidation. *ACS Appl. Mater. Interfaces* **2016,** *8* (23), 14527-14534.
54. Zhao, X.; Niu, C.; Zhang, L.; Guo, H.; Wen, X.; Liang, C.; Zeng, G., Co-Mn layered double hydroxide as an effective heterogeneous catalyst for degradation of organic dyes by activation of peroxymonosulfate. *Chemosphere* **2018,** *204*, 11-21.
55. Chen, D.; Chen, H.; Chang, X.; Liu, P.; Zhao, Z.; Zhou, J.; Xu, G.; Lin, H.; Han, S., Hierarchical CoMn-layered double hydroxide nanowires on nickel foam as electrode material for high-capacitance supercapacitor. *J. Alloys Compd.* **2017,** *729*, 866-873.
56. Su, D.; Tang, Z.; Xie, J.; Bian, Z.; Zhang, J.; Yang, D.; Zhang, D.; Wang, J.; Liu, Y.; Yuan, A.; Kong, Q., Co, Mn-LDH nanoneedle arrays grown on Ni foam for high performance supercapacitors. *Appl. Surf. Sci.* **2019,** *469*, 487-494.
57. Wang, D.; Li, J.; Zhang, D.; Liu, T.; Zhang, N.; Chen, L.; Liu, X.; Ma, R.; Qiu, G., Layered Co–Mn hydroxide nanoflakes grown on carbon cloth as binder-free flexible electrodes for supercapacitors. *J. Mater. Sci.* **2016,** *51* (8), 3784-3792.
58. Ochai-Ejeh, F. O.; Madito, M. J.; Momodu, D. Y.; Khaleed, A. A.; Olaniyan, O.; Manyala, N., High performance hybrid supercapacitor device based on cobalt manganese layered double hydroxide and activated carbon derived from cork (Quercus Suber). *Electrochim. Acta* **2017,** *252*, 41-54.
59. Zhang, N.; Ren, X.; Guo, Y.; Liu, Z.; Liu, Y., Impinging Stream–Rotating Packed-Bed Reactor Combination Coprecipitation Synthesis of Cobalt–Manganese-Layered Double Hydroxide for Electrode Materials. *Energy Technol.* **2019**.
60. Shannon, R. D.; Prewitt, C. T., Effective ionic radii in oxides and fluorides. *Acta Crystallogr., Sect. B: Struct. Sci.* **1969,** *25*, 925-946.
61. Biesinger, M. C.; Payne, B. P.; Grosvenor, A. P.; Lau, L. W. M.; Gerson, A. R.; Smart, R. S. C., Resolving surface chemical states in XPS analysis of first row transition metals, oxides and hydroxides: Cr, Mn, Fe, Co and Ni. *Appl. Surf. Sci.* **2011,** *257* (7), 2717-2730.
62. Nesbitt, H. W.; Banerjee, D., Interpretation of XPS Mn(2p) spectra of Mn oxyhydroxides and constraints on the mechanism of MnO 2 precipitation. *Am. Mineral.* **1998,** *83* (3-4), 305-315.
63. Banerjee, D.; Nesbitt, H. W., XPS study of reductive dissolution of birnessite by oxalate: Rates and mechanistic aspects of dissolution and redox processes. *Geochim. Cosmochim. Acta* **1999,** *63*, 3025-3038.
64. Shchukarev, A.; Korolkov, D., XPS Study of group IA carbonates. *CEJC* **2004,** *2*, 347.
65. Briois, V.; Cartier dit Moulin, C.; Verdaguer, M., . *Actualité Chimique* **2000,** *3*, 31-40.
66. Aouadi, M.; Fornasieri, G.; Briois, V.; Durand, P.; Bleuzen, A., Chemistry of Cobalt(II) Confined in the Pores of Ordered Silica Monoliths: From the Formation of the Monolith to the CoFe Prussian Blue Analogue Nanocomposite. *Chem. Eur. J.* **2012,** *18* (9), 2617-2623.
67. Iwai, Y.; Miura, A.; Rosero-Navarro, N. C.; Higuchi, M.; Tadanaga, K., Composition, valence and oxygen reduction reaction activity of Mn-based layered double hydroxides. *J. Asian Ceramic Soc.* **2019,** *7* (2), 147-153.
68. Li, B.; Gu, Z.; Kurniawan, N.; Chen, W.; Xu, Z. P., Manganese-Based Layered Double Hydroxide Nanoparticles as a T1-MRI Contrast Agent with Ultrasensitive pH Response and High Relaxivity. *Adv. Mater.* **2017,** *29* (29), 1700373.
69. Mills, S. J.; Christy, A. G.; Génin, J. M. R.; Kameda, T.; Colombo, F., Nomenclature of the hydrotalcite supergroup: natural layered double hydroxides. *Mineral. Mag.* **2012,** *76*, 1289-1336.
70. Britto, S.; Joseph, S.; Vishnu Kamath, P. J. J. o. C. S., Distinguishing crystallite size effects from those of structural disorder on the powder X-ray diffraction patterns of layered materials. *J. Chem. Sci.* **2010,** *122* (5), 751-756.
71. Zhitova, E. S.; Krivovichev, S. V.; Pekov, I.; Greenwell, H. C., Crystal chemistry of natural layered double hydroxides. 5. Single-crystal structure refinement of hydrotalcite, [Mg6Al2(OH)16](CO3)(H2O)4. *Mineral. Mag.* **2019,** *83* (2), 269-280.
72. Rouxhet, P. G.; Taylor, H. F. W., Thermal decomposition of sjoegrenite and pyroaurite. *Chimia* **1969,** *23*, 480-485.
73. Jayanthi, K.; Kamath, P. V., Observation of cation ordering and anion-mediated structure selection among the layered double hydroxides of Cu(ii) and Cr(iii). *Dalton Trans.* **2013,** *42* (36), 13220-13230.
74. Manohara, G. V.; Vishnu Kamath, P., Synthesis and structure refinement of layered double hydroxides of Co, Mg and Ni with Ga. *Bull. Mater. Sci.* **2010,** *33* (3), 325-331.
75. Shannon, R., Revised effective ionic radii and systematic studies of interatomic distances in halides and chalcogenides. *Acta Crystallogr., Sect. A: Found. Crystallogr.* **1976,** *32* (5), 751-767.
76. Taviot-Gueho, C.; Vialat, P.; Leroux, F.; Razzaghi, F.; Perrot, H.; Sel, O.; Jensen, N. D.; Nielsen, U. G.; Peulon, S.; Elkaim, E.; Mousty, C., Dynamic Characterization of Inter- and Intralamellar Domains of Cobalt-Based Layered Double Hydroxides upon Electrochemical Oxidation. *Chem. Mater.* **2016,** *28* (21), 7793-7806.
77. Kuo, C.-C.; Lan, W.-J.; Chen, C.-H., Redox preparation of mixed-valence cobalt manganese oxide nanostructured materials: highly efficient noble metal-free electrocatalysts for sensing hydrogen peroxide. *Nanoscale* **2014,** *6* (1), 334-341.
78. Su, C.-Y.; Lan, W.-J.; Chu, C.-Y.; Liu, X.-J.; Kao, W.-Y.; Chen, C.-H., Photochemical Green Synthesis of Nanostructured Cobalt Oxides as Hydrogen Peroxide Redox for Bifunctional Sensing Application. *Electrochim. Acta* **2016,** *190*, 588-595.
79. Ensafi, A. A.; Jafari–Asl, M.; Rezaei, B., A novel enzyme-free amperometric sensor for hydrogen peroxide

based on Nafion/exfoliated graphene oxide–Co3O4 nanocomposite. *Talanta* **2013,** *103*, 322-329.
80. Yao, S.; Yuan, S.; Xu, J.; wang, Y.; Luo, J.; Hu, S., A hydrogen peroxide sensor based on colloidal MnO2/Na-montmorillonite. *Appl. Clay Sci.* **2006,** *33* (1), 35-42.

TOC GRAPHIC